Research Article

Eliana Nope*, Gabriel Sathicq, José J. Martinez, Indry Milena Saavedra Gaona, Michael Castaneda Mendoza, Carlos Arturo Parra Vargas, Gustavo P. Romanelli, and Rafael Luque*

Cationic charge influence on the magnetic response of the Fe_3O_4–$[Me^{2+}_{1-y}Me^{3+}_{y}(OH_2)]^{y+}(Co_3^{2-})_{y/2}\cdot mH_2O$ hydrotalcite system

https://doi.org/10.1515/ntrev-2025-0204
received August 7, 2024; accepted July 11, 2025

Abstract: This work reports the influence of cationic charge on the magnetic response of hydrotalcites combined with magnetite nanoparticles. Fe_3O_4 particles were synthesized by the co-precipitation method, and the resulting magnetic particles were dispersed. A mixture of Mg, Me (Ni, Co, Sr), and Al nitrates with stoichiometric Me^{2+}/Me^{3+} molar ratios of 2 and 3 was added. X-ray diffraction patterns revealed the presence of Fe_3O_4 and hydrotalcite main phases and some secondary phases in the Sr^{2+}-modified sample. The FTIR spectra provided information on the chemical structure of the materials and confirmed the presence of representative vibrational bands for the composite structure. N_2 adsorption–desorption isotherms analyzed by the BET method indicated remarkable porous properties for the synthesized samples, and higher surface areas of 160 and 145 m^2/g were obtained for Fe_3O_4MgCoAl x = 3 and Fe_3O_4MgNiAl x = 3, respectively, with an increasing modifying cation ratio. The morphological characterization through SEM showed that a higher content of divalent cations favors the formation of larger particles, reaching a particle size of 786 nm for the sample with Ni^{2+} addition. The magnetic measurements showed marked ferromagnetic behavior with variations in saturation and remanent magnetizations due to the influence of modifying cations. The analysis revealed a correlation between the cationic charge and the magnetic and structural properties of the hydrotalcites, suggesting effective control over the magnetic properties by manipulating the cationic charge in these composite materials.

1 Introduction

Layered double hydroxides (LDHs) consist of layers similar to the brucite structure containing hydroxides of divalent metal cations (Me^{2+} = Mg, Co, Cu, Ni, Zn) and trivalent cations (Me^{3+} = Al, Fe, Ga) [1]. In the layered structure, each cation is octahedrally surrounded by six OH^- ions, and these octahedra share edges, forming a 2D layer. Exchange anions (An^- = CO_3^{2-}, Cl^-, NO_3^-, *etc.*) reside between these layers [2,3]. Substituting divalent cations with trivalent cations generates a positive charge balanced by interlayer anions, where water molecules also reside, bonded *via* hydrogen bonds to the OH^- layer and/or interlayer anions [4]. The layered structure emerges from electrostatic interactions and hydrogen bonding. These materials are described by the general formula $[Me^{2+}_{1-y}Me^{3+}_{y}(OH_2)]^{y}(A^{n-})_{\frac{y}{n}}\cdot mH_2O$, where y ranges from 0.25 to 0.33, indicating a Me^{2+}/Me^{3+} molar ratio of 2.0–4.0, and the water content (m) can be varied over a wide range. These characteristics provide the flexibility in tuning LDH composition, enabling the synthesis of materials with desired properties for specific studies or applications [5,6].

In recent years, hydrotalcites as multifunctional materials have received considerable attention due to their highly ordered lamellar structure and biocompatibility with low toxicity, presenting potential applications in

*** Corresponding author: Eliana Nope,** Universidad ECOTEC Km 13.5 Samborondón, Samborondón, 092302, EC; Centro de Investigación y Desarrollo en Ciencias Aplicadas "Dr. Jorge J. Ronco" (CINDECA-CCT La Plata-CONICET-CIC-PBA) Universidad Nacional de La Plata Calle 47 No 257, La Plata, B1900AJK, Argentina, e-mail: elianronova@gmail.com
*** Corresponding author: Rafael Luque,** Universidad ECOTEC Km 13.5 Samborondón, Samborondón, 092302, EC; Peoples Friendship University of Russia (RUDN University), 6 Miklukho Maklaya str., 117198, Moscow, Russian Federation, e-mail: rluque@ecotec.edu.ec
Gabriel Sathicq, Gustavo P. Romanelli: Centro de Investigación y Desarrollo en Ciencias Aplicadas "Dr. Jorge J. Ronco" (CINDECA-CCT La Plata-CONICET-CIC-PBA) Universidad Nacional de La Plata Calle 47 No 257, La Plata, B1900AJK, Argentina
José J. Martinez: Escuela de Ciencias Química Universidad Pedagógica y Tecnológica de Colombia Avenida Central del Norte, Tunja, 39–115, Colombia
Indry Milena Saavedra Gaona, Michael Castaneda Mendoza, Carlos Arturo Parra Vargas: Grupo Física de Materiales, Escuela de Física, Universidad Pedagógica y Tecnológica de Colombia, Tunja, Boyacá, 150003, Colombia

fields such as environmental protection [7], catalysis [8], biomedicine, and as adsorbents [1,9,10]. Moreover, owing to the abundant ionic surface (comprising hydroxyl groups) and the intrinsic positive charge possessed by these materials, the sheets can effectively engage with other nanomaterials or polymeric molecules. This interaction leads to the formation of 3D nanocomposites with distinct structures, such as Core@LDH, Shell@LDH, functionalized LDH, and LDH-coated structures. Within the core-layer architecture, the versatility and functionality of LDH serve a dual purpose: functioning as both the shell component for modifying other particles and as a core that can be coated with additional nanomaterials [2,11]. However, the separation and recovery of these materials in some processes is still difficult. Therefore, solid materials with magnetic properties can be easily separated by applying an external magnetic field, improving their recovery, and avoiding the loss of materials.

Magnetic nanoparticles are a popular research topic in a wide range of applications, such as targeted drug delivery, environmental remediation, magnetic resonance imaging, and catalysis [12–15]. Magnetic separation has been shown to be a promising, fast, simple, and highly effective method in solid–liquid phases. In addition, in the administration of drugs, they significantly facilitate the precise transfer of molecules to a specific site, without causing side effects in the human body, and their magnetic properties, such as superparamagnetic behavior, allow the transport of pharmaceuticals to be much more efficient [16,17].

Thus, several investigations have focused on the synthesis of magnetic hydrotalcites due to the properties of these materials and their layered nanostructures with high thermal and chemical stability [2,18]. They have been studied in targeted drug delivery processes, in the selective administration of chemotherapeutic agents, in the removal of toxic metal ions and dye treatments in wastewater, and as catalytic materials for obtaining platform molecules from lignocellulosic waste. Recently, Huang *et al.* [19] described the synthesis of a catalyst from reconstituted magnetic hydrotalcites with graphene quantum dots (GQDs) for efficient degradation of tetrachloroguaiacol (TeCG). The results showed that GQD provided greater thermal stability, surface area, and charge transferability with a removal efficiency of 89.34% within 60 min. These results highlight the potential of modified hydrotalcite-based materials modified to be applied to environmental remediation and water treatment. On the other hand, Hu *et al.* [20] carried out research on the CuO modification of hydrotalcites for the improvement of their nitrate adsorption ability in wastewater. The material was synthesized by using the impregnation method and was characterized with a high adsorption capacity of 102 mg/g. Moreover, the material showed good stability, and it retained more than 83% of its adsorption capacity after four regeneration cycles. These findings demonstrate the potential of modified hydrotalcites as an application in the treatment of water with nitrates. Structural modifications in hydrotalcites enable fine-tuning their properties and broadening their potential applications. Therefore, it is essential to analyze how the Me^{2+}/Me^{3+} ratio (where Me = Ni, Co, Sr) influences the structural and magnetic characteristics of hydrotalcites combined with Fe_3O_4 nanoparticles.

Magnetic hydrotalcites are generally synthesized by magnetic particle dispersion processes in the matrix of lamellar double hydroxides, where magnetic nanoparticles of magnetite (Fe_3O_4) or magnesium ferrite ($MgFe_2O_4$) are mainly used. The morphology of the sheets on the cores of the magnetic nanoparticles can form vertical, horizontal, or mixed orientations. This orientation will depend on the synthesis method, as well as the composition of the cations in the sheets and the solvent effect in the synthesis process [11,21,22]. In previous studies, we have observed that the synthesis of hydrotalcites with a double divalent cation or ternary hydrotalcites plays a crucial role in shaping the morphology of these materials [23]. However, the effect of the molar ratio of metal cations on the magnetic properties of Fe_3O_4 has been relatively underexplored.

Therefore, in this work, ternary magnetic hydrotalcites with varying *y*-values were synthesized in order to evaluate the impact of cationic loading on the magnetic and structural properties of these materials. Comprehensive characterizations were carried out using advanced techniques, including X-ray diffraction (XRD), to determine the crystal structure, vibrating sample magnetometry (VSM) to evaluate the magnetic properties, and N_2 adsorption–desorption isotherm analysis to investigate porosity and specific surface area. This approach allows a detailed correlation between the cation charge and the magnetic and structural properties of hydrotalcites, facilitating effective control of magnetic properties through precise manipulation of the molar ratio of divalent and trivalent cations.

2 Experimental

2.1 General information

All of the chemicals (such as $Mg(NO_3)_2{\cdot}6H_2O$, $Ni(NO_3)_2{\cdot}6H_2O$, $Co(NO_3)_2{\cdot}6H_2O$, $Sr(NO_3)_2{\cdot}6H_2O$, $Al(NO_3)_3{\cdot}9H_2O$, $FeCl_2{\cdot}6H_2O$, $FeCl_3{\cdot}6H_2O$, NaOH, and HNO_3) were purchased in analytical purity from Sinopharm Chemical Reagent (Beijing, China), and used without any further purification. The synthesis

process of the materials is illustrated in Figure 1. It begins with the preparation of Fe_3O_4 magnetic nanoparticles *via* the coprecipitation method, using ferric and ferrous iron salts in a basic aqueous solution. Once Fe_3O_4 is obtained, it is combined with the precursor salts of divalent and trivalent cations for the synthesis of hydrotalcite, also using the coprecipitation method, as described below.

2.2 Synthesis of Fe_3O_4 particles

Magnetic NPs were synthesized by the co-precipitation method using the methodology proposed by Kang *et al.* [24]. A molar ratio of Fe(II)/Fe(III) = 0.5 and pH = 11–12 were used. Briefly, 0.85 mL of 12.1 N HCl and 25 mL of purified, deoxygenated water (by nitrogen gas bubbling for 30 min) were combined, and 5.2 g of $FeCl_3$ and 2.0 g of $FeCl_2$ were successively dissolved in the solution with stirring. The resulting solution was added dropwise to 250 mL of 1.5 M NaOH solution under vigorous stirring, generating a black precipitate, which was then centrifuged at 400 rpm and washed with deoxygenated water. Subsequently, 500 mL of 0.01 M HCl was added to neutralize the anionic charges on the NPs. The solid was obtained by centrifugation, washed with distilled water, and then dried at 353 K.

The mechanism for the synthesis of Fe_3O_4 involves three key steps: (1) the dissociation of iron salts in aqueous solution (1), (2) the precipitation of iron hydroxides upon the addition of NaOH, and (3) a subsequent dehydration and redox process that leads to the formation of Fe_3O_4 [25,26]:

$$\begin{aligned} FeCl_3 &\leftrightarrow Fe^{3+} + 3Cl^- \\ FeCl_2 &\leftrightarrow Fe^{2+} + 2Cl^-, \end{aligned} \tag{1}$$

$$\begin{aligned} Fe^{3+} + 3OH^- &\rightarrow Fe(OH)_3\downarrow \\ Fe^{2+} + 2OH^- &\rightarrow Fe(OH)_2\downarrow, \end{aligned} \tag{2}$$

$$Fe(OH)_2 + 2Fe(OH)_3 \rightarrow Fe_3O_4 + 4H_2O. \tag{3}$$

2.3 Synthesis of magnetic ternary hydrotalcites

The synthesis of magnetic ternary hydrotalcites was carried out following the methodology proposed by Zhang *et al.* [22], using Fe_3O_4 as a magnetic source. For this, 1 g of Fe_3O_4 was dispersed in 100 mL of a water/methanol solution (V. water/V. methanol = 1/1, v/v), which was subjected to ultrasonification for 20 min to obtain a uniform suspension. Then, the pH was adjusted to 10 by adding a 2.0 M alkaline solution of Na_2CO_3 and NaOH. A mixture solution containing $Mg(NO_3)_2{\cdot}6H_2O$, $Me(NO_3)_2{\cdot}6H_2O$, and $Al(NO_3)_3{\cdot}9H_2O$ with a Me^{2+}/Al^{3+} = 2 and 3 ratio (Me = Ni, Co, Sr) with y = 0.33 and 0.25, respectively, was added dropwise to the suspension and aged at 140°C for 24 h. The resulting solid was separated magnetically, washed with deionized water, and dried at 80°C overnight. The materials are denoted as Fe_3O_4–MgCoAl x = 3, Fe_3O_4–MgNiAl x = 3, Fe_3O_4–MgSrAl x = 3, Fe_3O_4–MgCoAl x = 2, Fe_3O_4–MgNiAl x = 2, and Fe_3O_4–MgSrAl x = 2. In addition, Fe_3O_4–MgAl x = 3 and Fe_3O_4–MgAl x = 2 were synthesized as control samples, where x represents the Me^{2+}/Me^{3+} ratio, 2 and 3.

Hydrotalcite is synthesized with a [urea]/[NO_3^-] molar ratio of 3. The carbonate generated from urea decomposition acts as a compensating anion in the amine phase of hydrotalcite [27], with the following reaction mechanism:

$$\begin{aligned} NH_2 - CO - NH_2 + 3H_2O &\rightarrow NH_4^+ + CO_3^{2-} \\ (NH_4)_2CO_3 &\rightarrow 2NH_3\uparrow + CO_2\uparrow + H_2O \\ NH_3 + H_2O &\leftrightarrow NH_4OH \leftrightarrow NH_4^+ + OH^- \\ CO_2 + H_2O &\leftrightarrow H_2CO_3 \leftrightarrow H^+ + HCO_3^- \leftrightarrow 2H^+ + CO_3^{2-} \\ OH^- + (1-y)Mg^{2+} + yAl^{3+} + \left(\frac{y}{2}\right)CO_3^{2-} &+ mH_2O \rightarrow [Mg_{1-y}Al_y(OH)_2](CO_3)_{\frac{y}{2}}{\cdot}mH_2O \\ 18OH^- + 6Mg^{2+} + 2Al^{3+} + 9CO(NH_2)_2 &+ 12H_2O \rightarrow Mg_6Al_2(OH)_{16}CO_3{\cdot}4H_2O + 18NH_3 + 8CO_2. \end{aligned} \tag{4}$$

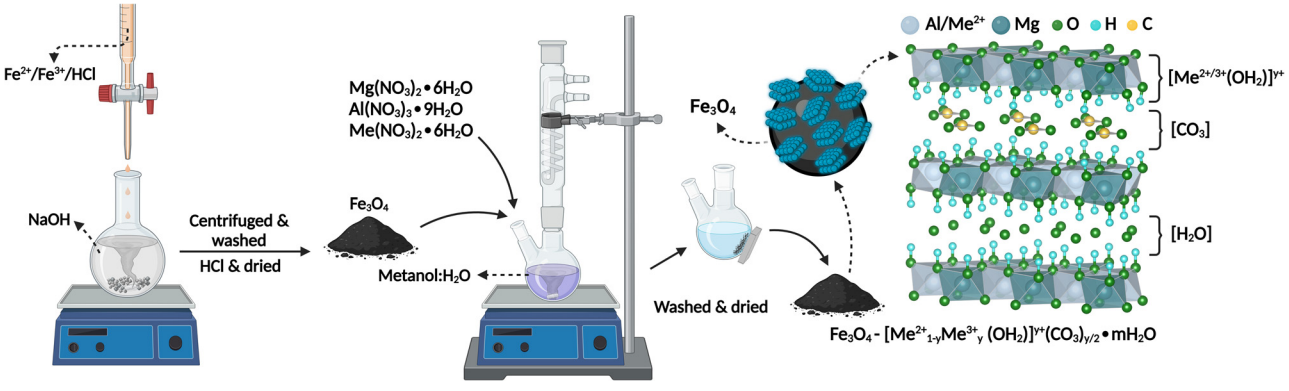

Figure 1: Schematic synthesis of the magnetic hydrotalcite samples with Me^{2+}/Me^{3+} molar ratios using the coprecipitation method.

A 2M alkaline solution of NaOH and Na_2CO_3 (1:1 molar ratio) was prepared by dissolving NaOH in distilled water, followed by the gradual addition of Na_2CO_3 until the final volume was reached. The mixture was stirred continuously until a homogeneous, translucent solution was obtained.

2.4 Characterization

The XRD patterns and crystalline phases were recorded with a Panalytical X´pert PRO-MPD equipment with an ultrafast X´Celerator detector in Bragg–Brentano geometry, using Copper Cu-K_α radiation (λ = 1.54056 Å), 2θ = 10–90° with a step of 0.0263°, and a capture time of 100 s. The patterns were analyzed with the General Structure Analysis System (GSAS II) software. Fourier-transform infrared (FTIR) spectra were recorded on a Nicolet iS50 spectrometer in the range of 4,500–600 cm^{-1} using pressed KBr pellets. Morphology properties of the compounds were evaluated by SEM (JSM 6610-LV JEOL equipment). The Brunauer–Emmett–Teller (BET) isotherm and Barrett, Joyner, and Halenda (BJH) method were used to calculate the specific surface area and pore volume, respectively, and N_2 adsorption–desorption isotherms of the solids were measured at 77 K (Micromeritics ASAP 2020 equipment). The samples were previously degassed at 100°C under vacuum for 18 h. The magnetic measurements were developed using a VSM Quantum Design. The measurements as a function of temperature were carried out in the temperature range of 50–300 K using the zero-field cooled–field cooled (ZFC-FC) mode.

3 Results and discussion

3.1 Structural analysis

The XRD patterns of the synthesized samples (Figure 2) showed characteristic peaks corresponding to the crystal structure of hydrotalcite. The most prominent peak was observed around 11.6° 2θ, which is assigned to the (003) plane diffraction, confirming the formation of the hydrotalcite phase [3]. All of the samples were contrasted with the hexagonal phase of hydrotalcite with space group $P\bar{6}2m$ (189) and JCPDS card No. 22-0452, and thus being able to determine the presence of this phase, which by the shape of the signals, tends to have a nanometric nature

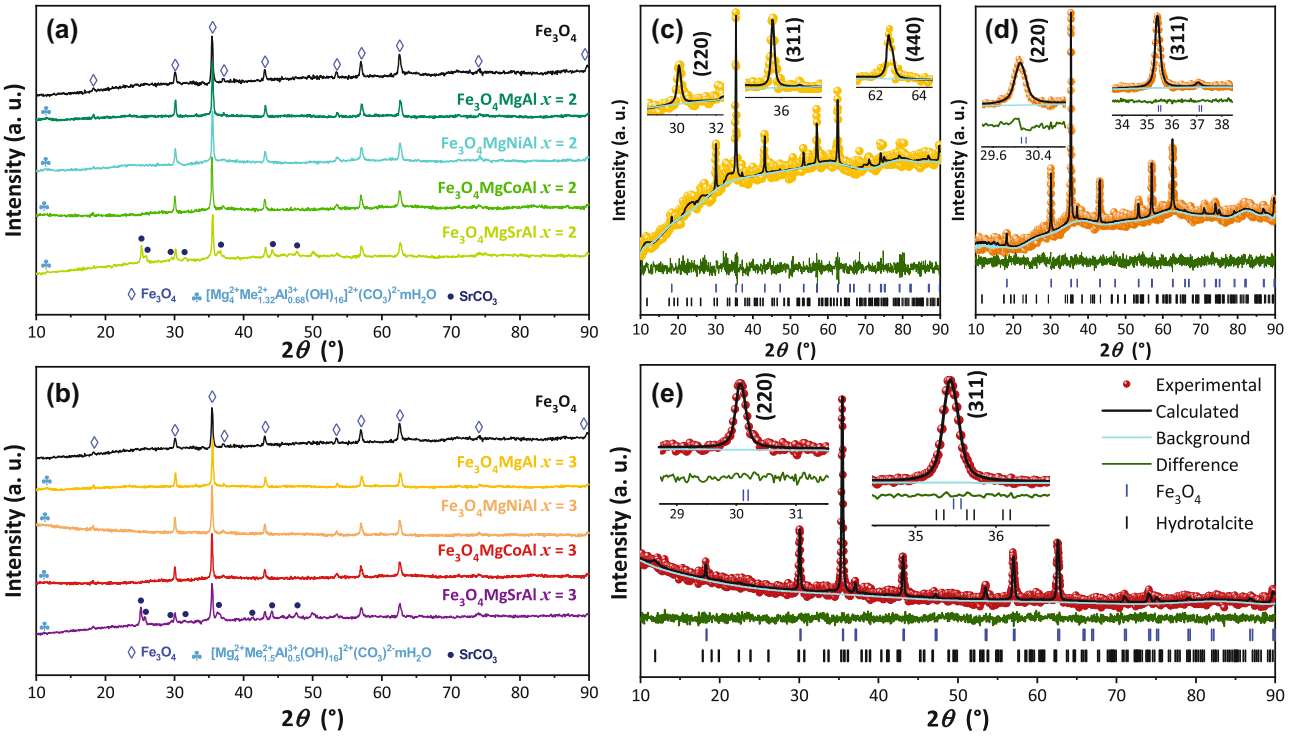

Figure 2: XRD patterns of the Fe_3O_4MgAl magnetic hydrotalcite with molar ratios of (a) x = 2 and (b) x = 3. Rietveld refinements for (c) Fe_3O_4MgCoAl x = 2, (d) Fe_3O_4MgCoAl x = 3, and (e) Fe_3O_4MgNiAl x = 3 samples. The experimental pattern, calculated profile, and Bragg peak positions are indicated by circles, a black curve, and tick marks, respectively. The bottom curve shows the difference between the observed and calculated intensities.

Table 1: Structural parameters of the magnetic hydrotalcite samples with Me^{2+}/Me^{3+} molar ratios (*W* (%) is the weight percentage of each sample)

Sample	$\frac{Me^{2+}}{Me^{3+}}$	χ^2	R^2	Fe_3O_4						Hydrotalcite							
				W (%)	*a* = *b* = *c* (Å)	*V* (Å^3)	CS (nm)			*W* (%)	*a* = *b* (Å)	*c* (Å)	*V* (Å^3)	Cs (nm)			
							2*θ* (°)	Sch	*L*(||)	*L*(⊥)					2*θ* (°)	Sch	*L*(||)	*L*(⊥)
Fe_3O_4	—	0.826	0.161	100.00	8.397	592.15	35.44	33.40	65.55	59.69	—	—	—	—	—	—	—	—
Fe_3O_4MgAl	2	1.220	0.184	79.64	8.385	589.49	35.46	34.24	50.77	50.62	20.360	5.228	15.090	412.38	11.65	16.39	15.00	15.80
	3	1.051	0.232	77.58	8.386	589.77	35.49	48.64	57.05	55.95	22.420	5.283	15.150	422.84	11.50	10.19	15.05	15.05
Fe_3O_4MgCoAl	2	0.684	0.100	81.81	8.387	589.87	35.51	41.77	48.02	52.09	18.187	5.392	15.067	438.03	11.67	13.33	3.82	3.86
	3	0.774	0.192	89.39	8.388	590.25	35.40	48.63	48.92	54.92	10.607	5.291	15.173	424.73	12.01	108.63	3.10	4.29
Fe_3O_4MgNiAl	2	0.904	0.206	64.41	8.386	589.79	35.50	41.76	47.47	44.98	35.587	5.235	14.972	410.34	11.51	9.99	5.58	1.87
	3	0.772	0.188	74.74	8.386	589.74	35.41	48.63	59.15	69.09	25.260	5.410	14.922	436.79	11.62	92.67	8.35	12.84
Fe_3O_4MgSrAl	2	0.888	0.154	59.99	8.391	590.82	35.53	41.77	59.59	42.50	5.342	5.264	15.074	417.69	11.74	92.68	7.79	5.74
	3	0.985	0.221	41.35	8.390	590.63	35.44	33.40	43.09	43.45	27.538	5.280	15.228	424.46	11.09	92.63	2.40	2.35

with a limit to amorphousness [28,29]. When the diffraction patterns of the different samples were compared, a slight variation in the peak positions and their relative intensities was observed (Table 1). This variation suggests that the molar ratio of metal cations influences the interlayer distance and crystalline ordering. The experimental patterns confirmed the absence of secondary phases in the samples, except for the Sr^{2+} inclusion sample (Figure 2a and b), where a significant presence of $SrCO_3$ was detected [30].

Additionally, the presence of high-intensity peaks around 30°, 35°, 43°, 53°, 57° and 62° 2θ in all samples indicates the coexistence of Fe_3O_4 particles embedded in the hydrotalcite matrix, corresponding to the (220), (311), (440), (422), (511), and (440) diffraction planes, respectively. This phase was indexed to the cubic Fe_3O_4 phase with space group $Fd\bar{3}m$ (JCPDS 19-0629). The presence of these signals, considering the synthesis process followed, allows corroborating the successful integration of the magnetic particles on the hydrotalcite structure or the other way around. This observation is supported by the identification of both crystalline phases by XRD, which allows confirming the homogeneous and effective integration of Fe_3O_4 nanoparticles within the hydrotalcite matrix [31,32].

The crystallite size (CS) of the present phases in the materials was also calculated using the Debye–Scherrer equation (5) [33,34],

$$\mathrm{CS} = \frac{K\lambda}{\beta \cos\theta}, \tag{5}$$

where $K = 0.94$ is the Scherrer form factor, $\lambda = 0.1542$ nm is the Cu cathode radiation, β is the full width at half-maximum of the peaks, and θ is the Bragg diffraction angle. The diffraction planes used to determine CS were (003) for the hydrotalcite phase and (311) for the Fe_3O_4 phase. Table 1 summarizes the findings. The CS for the Fe_3O_4 phase showed an increase when it coexisted with hydrotalcites with an Me^{2+}/Me^{3+} ratio of 3. These hydrotalcites showed variable CS, with a tendency to increase as the molar ratio increases to $x = 3$.

Rietveld refinement was carried out (using GSAS-I software [35–37]) to determine complementary structural properties of the acquired samples and their present phases. The lattice parameters and unit cell volume may be obtained using the established refinement procedure. These, along with other important factors, are provided in Table 1. Figure 2c and d shows the plots created for the refinement of some samples. This research demonstrates that the materials crystallized in a hexagonal and cubic form, for hydrotalcite and Fe_3O_4 phases, respectively, which is consistent with earlier semi-quantitative investigations [31,32], as evidenced by the overlap of theoretical

and experimental patterns. All the samples have lattice parameters close to 8.386 Å, which is consistent with a spinel-type structure. Quantitative analysis of the phase percentage in the synthesized samples revealed significant variation in the distribution of Fe_3O_4 and hydrotalcite. The percentages of Fe_3O_4 ranged from 41.35 to 89.39%, while those of hydrotalcite ranged from 5.34 to 35.59%. This variability suggests that the synthesis conditions strongly influence the phase structure and ratio, thereby affecting the physical and chemical properties of the composite material. The sample Fe_3O_4MgNiAl (x = 2) exhibits the highest content of hydrotalcite (35.59%), followed by Fe_3O_4MgNiAl (x = 3) with 25.26%. On the other hand, the samples Fe_3O_4MgSrAl (x = 2) and Fe_3O_4MgCoAl (x = 3) show the lowest contents of hydrotalcite (5.34 and 10.61%, respectively). This suggests that the addition of Sr and Co particularly stabilizes the spinel phase, significantly reducing the amount of hydrotalcite formed. In contrast, Ni appears to promote the formation of hydrotalcite due to its influence on the stability of lamellar phases, while Sr and Co seem to better stabilize the spinel-type structure.

A higher Fe_3O_4 content could favor magnetic properties, while a higher proportion of hydrotalcite could enhance catalytic and adsorption properties. The ability to adjust these ratios is crucial for the optimization of the material for specific applications. Furthermore, Rietveld crystallite sizes were also estimated in both perpendicular $L(\perp)$ and parallel $L(\parallel)$ directions with equations (6) and (7), based on GSAS revised Lorentzian component parameters (LX and ptec), and K and λ correspond to Scherrer parameters [38,39]. The samples reveal significant variation in $L(\parallel)$ and $L(\perp)$ parameters, suggesting a direct effect of composition on structural anisotropy. In the pure Fe_3O_4 sample, $L(\parallel)$ and $L(\perp)$ have values of 65.55 and 59.69 nm, respectively, indicating slight anisotropy in crystal growth. With the addition of the basal hydrotalcite, Fe_3O_4MgAl sample, both parameters decrease, reaching values of 55.92 and 55.07 nm, suggesting that the addition of the hydrotalcites limits the growth of the crystalline domains [40]. In general, a decrease of these parameters was observed in the Fe_3O_4 phase, reaching a minimum in the Fe_3O_4MgSrAl sample. The samples Fe_3O_4MgCoAl x = 3 and Fe_3O_4MgNiAl x = 3 exhibit the largest crystallite sizes, suggesting better crystallization or lower stresses in the lattice. For the hydrotalcite phase, these parameters presented a notable decrease with the addition of the substituent cations, reflecting a more restricted structure in terms of crystal growth and a limitation in the crystalline development with these compositional modifications. In general, the incorporation of different cations influences the size and preferential orientation of crystallite growth, which can directly impact their structural and functional properties.

$$L(\perp) = \frac{1{,}800K\lambda}{\pi LX}, \tag{6}$$

$$L(\parallel) = \frac{1{,}800K\lambda}{\pi(LX + \text{ptec})}. \tag{7}$$

In general, all systems exhibited a spinel structure obtained through various synthesis methods. Most of the methods reported in the literature produce crystallites with sizes similar to those obtained in this study. For instance, the compounds $Zn_{1-x}Ni_xFe_2O_4$, synthesized by sol–gel, sol–gel auto-combustion, microwave combustion, auto-combustion, thermal decomposition, and chemical co-precipitation methods, exhibited crystallite sizes ranging from 18 to 70 nm, depending on the synthesis technique used [41].

Magnesium plays a significant role in determining the crystal size of the synthesized materials (Table 1). The incorporation of Mg^{2+} into the spinel structure, either alone or in combination with other cations (such as Ni^{2+}, Co^{2+}, Sr^{2+}, and Al^{3+}), has a marked effect on the crystallite size and stability of the resulting phase. The incorporation of magnesium generally leads to a slight reduction in the crystal size compared to pure Fe_3O_4. This slight reduction in the crystal size is probably due to the substitution of Fe^{2+} and Fe^{3+} ions by Mg^{2+}, which has a smaller ionic radius (0.72 Å) compared to Fe^{2+} (0.78 Å). This substitution can induce local distortions in the crystal lattice, which hinders crystal growth and favors the formation of smaller crystallites.

The effect of the (Mg + Me)/Al ratio on the crystallite size of hydrotalcite could be explained in terms of the presence of cations. The presence of a larger number of trivalent cations (Al^{3+}) in the layers enhances the rate of stacking of the layers [42]. Samples containing only magnesium exhibit an (Mg/Al) = 1 ratio, while those combining magnesium with another divalent cation (Ni, Co, Sr) show a higher ratio of 2. This implies that samples with a higher (Mg + Me)/Al ratio have a greater proportion of divalent cations relative to trivalent cations, which may affect the crystallite size and the stability of the lamellar phase due to the lower positive charge density in the layers.

On the other hand, there is a noticeable variation in the hydrotalcite lattice parameters, which is associated with the crystalline development due to the chemical modification. Finally, regarding the parameter Chi (χ^2), it can be concluded that the Rietveld refinements made for the samples obtained were adequate, given the structural conditions exhibited by both phases in the samples. In addition, the R^2 parameter, as another reliability indicator, also makes it possible to corroborate the accuracy and validity of the refinement process.

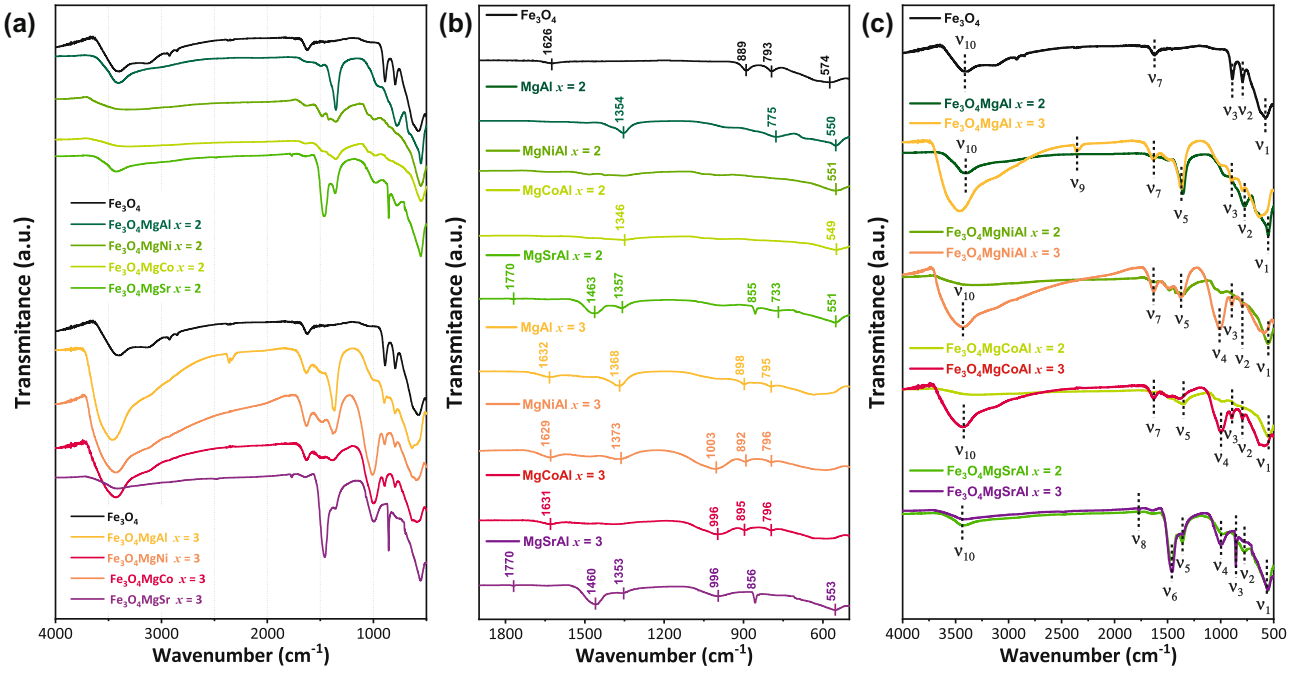

Figure 3: (a) and (b) FTIR spectra of the magnetic hydrotalcite samples with Me^{2+}/Me^{3+} molar ratios of 2 and 3; (c) Me^{2+}/Me^{3+} comparisons on the IR spectra of hydrotalcites. The dotted lines indicate the main bond vibrations.

The IR spectra of hydrotalcites show variable vibrational bands assigned to high (greater than 2,000 cm^{-1}), middle (2,000–1,000 cm^{-1}), and low (below 1,000 cm^{-1}) frequency ranges. The infrared spectra reveal distinctive features in the materials synthesized with Me^{2+}/Me^{3+} molar ratios of 2 and 3. These spectra resemble those of hydrotalcite and magnetic Fe_3O_4 nanoparticles. In Figure 3 and Table 2, a broad adsorption band with a maximum at 549–574 cm^{-1} (ν_1) corresponds to Fe–O bond stretching vibrations [31,32]. The stretching of Al–OH may be responsible for the bands at 667 and 733 cm^{-1} (ν_2). The band at 795 cm^{-1} (ν_2) is attributed to symmetric and antisymmetric vibrations of the Fe–O–H bond, characteristic of magnetic nanoparticles [32,43,44]. The weak band at 870 cm^{-1} (ν_3) was due to the characteristic O–C–O bond stretching vibrations of bidentate carbonate [45]. These signals are less intense in the synthesized ternary magnetic hydrotalcites, suggesting a potential core–shell structure, with the external layer of the hydrotalcite shielding the absorption of the Fe–O bond in the Fe_3O_4 phase [46]. The bands at 855 and 856 cm^{-1} (ν_3) are assigned to $SrCO_3$ bending vibrations in Fe_3O_4-MgSrAl sample [47,48]. These results indicate that

Table 2: Frequencies of absorption maxima (ν, cm^{-1}) in the IR spectra of magnetic hydrotalcite with molar ratios of Me^{2+}/Me^{3+}

Sample	Fe_3O_4	Fe_3O_4MgAl		Fe_3O_4MgNiAl		Fe_3O_4MgCoAl		Fe_3O_4MgSrAl		Atomic vibrations
Me^{2+}/Me^{3+}	–	2	3	2	3	2	3	2	3	
ν_1 (cm^{-1})	574	550	—	551	—	549	—	551	553	Fe–O stretching vibrations [32]; Al–O–Al [44]
ν_2 (cm^{-1})	793	775	795	—	796	—	796	773	—	Fe–O–H vibration; Al–OH translation [53]; Al–O [44]
ν_3 (cm^{-1})	889	—	898	—	892	—	895	855	856	O–C–O stretching vibrations [45]; Sr–O bending vibrations [46]
ν_4 (cm^{-1})	—	—	—	—	1003	—	996	—	996	Me–O–Me [46]
ν_5 (cm^{-1})	—	1,354	1,368	—	1,373	1,346	—	1,357	1,353	CO_3^{2-}/NO_3^- vibrations [49], [46];
ν_6 (cm^{-1})	—	—	—	—	—	—	—	1463	1,460	CO_3 symmetric and antisymmetric stretching [51]
ν_7 (cm^{-1})	1,626	—	1,632	—	1,629	—	1,631	—	—	H_2O [52], O–H bending vibration [53]
ν_8 (cm^{-1})	—	—	—	—	—	—	—	1,770	1,770	H_2O [54]
ν_9 (cm^{-1})	—	—	2,352	—	—	—	—	—	—	NO_3^- vibration [55]
ν_{10} (cm^{-1})	3,403	3,406	3,467	—	3,427	—	3,435	3,422	3,414	OH stretching vibration [44]; Me–OH [46]

the incorporation of magnetic nanoparticles into the hydrotalcite does not alter the laminar structure, whereas changes in the Me^{2+}/Me^{3+} molar ratio influence the formation of this structure. The band around 1,000 cm^{-1} (ν_4) represents the Me–O–Me skeletal vibrations and is pronounced in materials with Ni^{2+}, Co^{2+}, and Sr^{2+} [46]. However, this intensity is influenced by the Me^{2+}/Me^{3+} molar ratio in brucite-like lamellar layers, being lower in ternary magnetic hydrotalcite due to the presence of another divalent cation. In addition, the absorption band around 1,369 cm^{-1} (ν_5) was considered to be caused by the asymmetric stretching bond of the intercalated NO_3 [46,49] and by asymmetric vibrations of the CO_3^{2-} anion in the interlayer space of the hydrotalcite [50].

The presence of $SrCO_3$ in the Sr-modified samples generated a vibration band at 1,463 cm^{-1} (ν_6) due to the CO_3 symmetric and antisymmetric stretching [51]. In addition, an intense absorption peak at 1,460 cm^{-1} (ν_6) was attributed to the bending mode of the –OH groups of the adsorbed water interlayer [45]. The absorption band around 1,626 and 1,632 cm^{-1} (ν_7) was caused by the bending oscillation peaks of water molecules between layers [52,53]. The bending vibration of the interlayer water occurs at 1,700 cm^{-1} (ν_8) [54]. The band at 2,352 cm^{-1} (ν_9) was observed at high-frequency range and corresponded to NH_3^- [55].

The presence of vibrations at 3,403–3,467 cm^{-1} (ν_{10}), which indicate the presence of OH stretching vibration of the hydroxyl group in Mg–Al hydrotalcite [44], was caused by the water molecules between the layers of the laminar structure [56]. This shift is attributed to the ratio and not to the presence of magnetic nanoparticles. Additionally, characteristic vibrations of the hydrotalcite exhibit a slight shift to higher frequencies 3,467 (x = 3) – 3,414 (x = 2) cm^{-1} (ν_{10}), attributed to the symmetric stretching of the hydroxyl group linked to the Me–OH bond on the surface of the hydrotalcite [53].

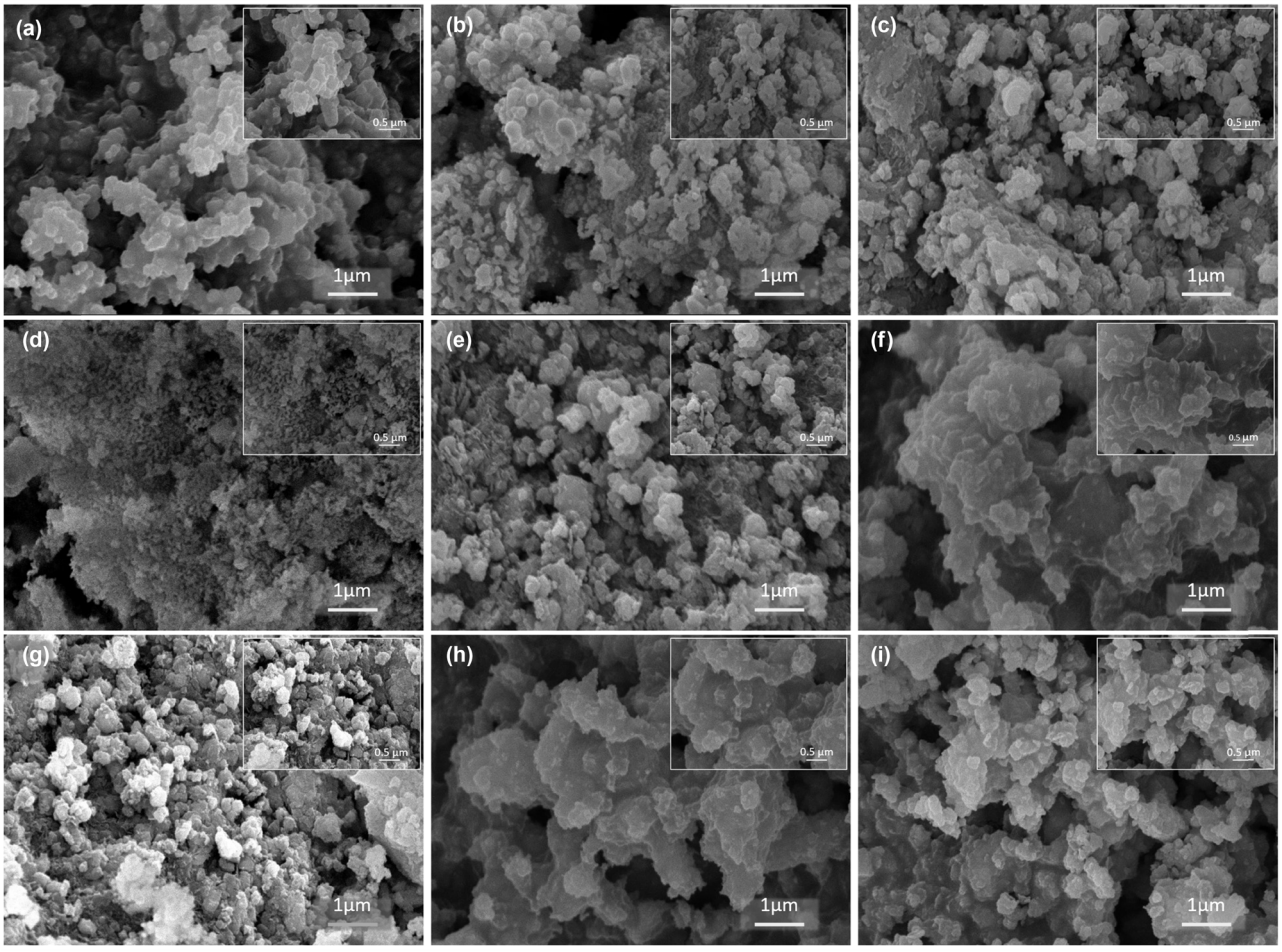

Figure 4: SEM images at 15 kx and 30 kx (insets): (a) Fe_3O_4, (b) Fe_3O_4MgCoAl x = 2, (c) Fe_3O_4MgCoAl x = 3, (d) Fe_3O_4MgAl x = 2, (e) Fe_3O_4MgNiAl x = 2, (f) Fe_3O_4MgNiAl x = 3, (g) Fe_3O_4MgAl x = 3, (h) Fe_3O_4MgSrAl x = 2, and (i) Fe_3O_4MgSrAl x = 3.

3.2 Morphological characterization

SEM images of the synthesized samples were obtained at magnifications of 15 kx and 30 kx (Figure 4). The Fe_3O_4 sample (Figure 4a) exhibits a granular morphology with spherical particles of uniform size, approximately 220 nm in diameter, indicating a controlled and homogeneous synthesis. A more complex structure with aggregated particles is observed in the Fe_3O_4MgCoAl $x = 2$ (Figure 4b) and $x = 3$ (Figure 4c) samples. The particles form larger agglomerates, increasing the surface roughness and porosity due to the presence of hydrotalcite, possibly attributed to the semi-amorphous matrix observed. The Fe_3O_4MgAl $x = 2$ (Figure 4d) and $x = 3$ (Figure 4g) images show a heterogeneous agglomerated structure, characteristic of hydrotalcites. The sample with $x = 2$ exhibits higher porosity and a more heterogeneous distribution of nanoparticles, suggesting a more intense interaction between the particles and the hydrotalcite matrix. The Fe_3O_4MgNiAl $x = 2$ (Figure 4e) and $x = 3$ (Figure 4f) micrographs demonstrate a more compact morphology for the sample $x = 3$. The Fe_3O_4 nanoparticles are uniformly distributed in both samples, although a slight tendency to agglomeration is observed in $x = 3$, causing larger agglomerates and difficult to perceive edges. Finally, the Fe_3O_4MgSrAl $x = 2$ (Figure 4h) and $x = 3$ (Figure 4i) images reveal a granular morphology with larger and less defined particles compared to the other samples. The presence of $SrCO_3$ seems to significantly affect the structure, increasing the particle size and surface roughness. The distribution of Fe_3O_4 nanoparticles is less uniform, with a tendency to agglomerate formation for the sample $x = 3$. SEM analysis shows that the composition and molar ratio of metal cations significantly influence the morphology and distribution of Fe_3O_4 nanoparticles. These variations allow control of the morphological and structural properties of the material, which is crucial for its optimization of its potential surface applications. In general, the synthesized hydrotalcite samples show zones with irregular plate-like morphology agglomerations, which highlights the inherent characteristics of the layered materials, such as a high surface-to-volume ratio and a structural arrangement that favors the intercalation of ions and molecules. These results are comparable with previous reports [31,57].

The calculated grain sizes for all systems are shown in Table 3. The Me^{2+}/Me^{3+} ratio has a remarkable relationship with the particle size of the samples [58]. For the sample Fe_3O_4 (without metal addition), the particle size is 220.5 ± 72.3 nm, indicating a relatively large and less controlled structure, without the intervention of divalent or trivalent metals. In the case of Fe_3O_4MgAl ($x = 2$, $Me^{2+}/Me^{3+} = 2$), the particle size decreases to 119.7 ± 59.2 nm, suggesting that the addition of Mg^{2+} and Al^{3+} favors further nucleation, reducing agglomeration and promoting smaller particles. However, when the ratio of Me^{2+}/Me^{3+} in Fe_3O_4MgAl is increased ($x = 3$, $Me^{2+}/Me^{3+} = 3$), the particle size increases to 224.3 ± 86.1 nm, suggesting that a higher Me^{2+} content could favor the formation of larger particles due to a lower crystallization rate or higher agglomeration. In Fe_3O_4MgCoAl ($x = 2$, $Me^{2+}/Me^{3+} = 2$), the particle size is 180.7 ± 87.9 nm, showing an intermediate value between the Fe_3O_4 and Fe_3O_4MgAl ($x = 2$) samples. This size could indicate a moderate control on particle nucleation and growth, favored by the addition of Co^{2+}. As the Me^{2+}/Me^{3+} ratio is increased to 3 in Fe_3O_4MgCoAl ($x = 3$), the particle size increases to 206.1 ± 76.5 nm, suggesting increased particle agglomeration due to the higher Me^{2+} content. In Fe_3O_4MgNiAl ($x = 2$, $Me^{2+}/Me^{3+} = 2$), the particle size is 235.8 ± 167.2 nm, which is considerably larger than in Fe_3O_4MgAl ($x = 2$), which might reflect the influence of Ni^{2+} on the formation of larger particles. Fe_3O_4MgNiAl ($x = 3$, $Me^{2+}/Me^{3+} = 3$) exhibits the largest particle size of 785.9 ± 554.9 nm, suggesting that the higher proportion of Me^{2+} favors higher agglomeration or weaker crystallinity, resulting in larger and less homogeneous

Table 3: BET analysis results of Fe_3O_4MgAl magnetic hydrotalcite with molar ratios of Me^{2+}/Me^{3+}

Sample	Me^{2+}/Me^{3+}	SEM particle size (nm)	S_{BET} (m^2/g)	Pore volume (cm^3/g)	Pore size (nm)
Fe_3O_4	—	220.5 ± 72.3	17	0.04	3
Fe_3O_4MgAl	2	119.7 ± 59.2	52	0.42	29
	3	224.3 ± 86.1	96	0.41	14
Fe_3O_4MgCoAl	2	180.7 ± 87.9	33	0.16	17
	3	206.1 ± 76.5	160	0.23	8
Fe_3O_4MgNiAl	2	235.8 ± 167.2	19	0.16	24
	3	785.9 ± 554.9	145	0.25	7
Fe_3O_4MgSrAl	2	763.6 ± 260.3	6	0.35	36
	3	258.9 ± 50.8	2	0.19	32

particles. Finally, the Fe_3O_4MgSrAl samples present an interesting behavior: in Fe_3O_4MgSrAl (x = 2, Me^{2+}/Me^{3+} = 2), the particle size is 763.6 ± 260.3 nm, indicating larger agglomeration, while at Fe_3O_4MgSrAl (x = 3, Me^{2+}/Me^{3+} = 3), the particle size is reduced to 258.9 ± 50.8 nm, suggesting that the addition of Sr^{2+} at this ratio may promote better formation of smaller and less agglomerated particles.

The textural properties of the synthesized materials were assessed through N_2 adsorption–desorption isotherms at 77 K, using the BET method, as shown in Figure 5. The adsorption isotherms of type III can be observed in the Sr samples. This classification is indicative of materials with limited microporosity or low porosity. This result suggests the potential partial formation of a laminar structure in these materials, possibly due to the presence of $SrCO_3$, which was identified through FTIR and XRD analysis. Conversely, for the remaining materials, type IV isotherms were observed, characteristic of mesoporous materials, with a H3 type hysteresis loop. This pattern is typical in materials with plate-like particles and slit-shaped mesopores, which is a common feature in hydrotalcite-like materials [46,50].

Table 3 presents the parameters of the pore structure of the synthesized materials, including the specific surface area (S_{BET}), pore volume, and pore size. The results reveal that different Me^{2+}/Me^{3+} molar ratios lead to significant changes in textural properties. Materials with a Me^{2+}/Me^{3+} molar ratio of 3 exhibit higher surface areas (S_{BET}) compared to those with an Me^{2+}/Me^{3+} ratio of 2. Thus, adjusting the ratio of metallic cations increases the pore size, leading to a decrease in the surface area. The pore size in all materials ranges from 3 to 36 nm, confirming the presence of mesopores in the laminar structure. These results indicate that the presence of magnetic nanoparticles does not impact the textural properties of the materials, and Fe_3O_4 acts as a magnetic separation agent. Furthermore, the potential core–shell structure seems to be favored at an Me^{2+}/Me^{3+} ratio of 3, as these materials present a larger surface area, suggesting better coverage of Fe_3O_4 with the hydrotalcite. The Fe_3O_4MgNiAl and Fe_3O_4MgCoAl samples with Me^{2+}/Me^{3+} of 3 showed a greater surface area, which is possibly associated with the nature of the synthesis that involves a heat of the

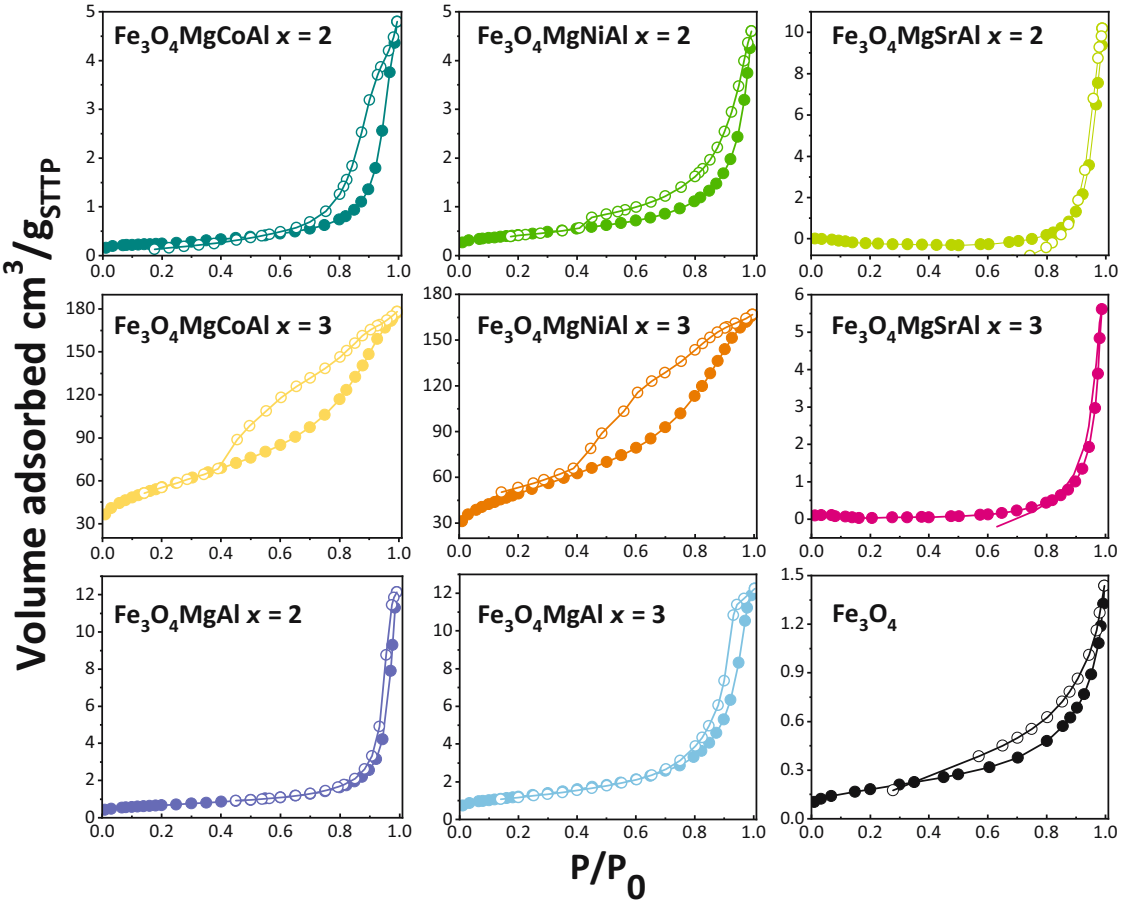

Figure 5: N_2 adsorption–desorption isotherms of Fe_3O_4MgAl magnetic hydrotalcite with molar ratios of Me^{2+}/Me^{3+}.

suspension, which favors the simultaneous nucleation of the crystals [59].

The samples with the largest surface area are Fe_3O_4MgCoAl (x = 3) (160 m^2/g) and Fe_3O_4MgAl (x = 3) (96 m^2/g), which is consistent with a larger pore volume. This higher S_{BET} could be related to higher particle dispersion and greater accessibility to active sites. On the contrary, the samples with lower surface area are Fe_3O_4 (17 m^2/g) and Fe_3O_4MgSrAl (x = 3) (2 m^2/g), which also present a reduced pore volume, suggesting that the incorporation of certain metals favors particle compaction and reduces the surface area available for interactions.

A trend is observed in which samples with a larger particle size (such as Fe_3O_4MgNiAl (x = 3) with 785.9 ± 554.9 nm) also have a reduced surface area (145 m^2/g) and a smaller pore volume. This suggests that larger particle size may be related to lower surface accessibility and less porous structure. On the other hand, samples with a smaller particle size, such as Fe_3O_4MgAl (x = 2), show a larger surface area (52 m^2/g) and significant pore volume (0.42 cm^3/g), indicating greater exposure to active sites and greater potential for applications where high surface area availability is required.

3.3 Magnetic characterization

The magnetic behavior of the synthesized hydrotalcite-type materials was analyzed by magnetization as a function of magnetic field curves at 50 K (low temperature) and 300 K (room temperature). All samples showed narrow S-shape type loops (Figure 6), indicating a superparamagnetic behavior with no significant changes observed in the magnetic curves across 50 K. The magnetic saturation (M_s), remanence magnetization (M_r), and coercivity field (H_c) values calculated from magnetically recorded data are listed in Table 4. The M_s values exhibit notable variations depending on the Me^{2+}/Me^{3+} ratio and the analysis temperature. Notably, Table 4 shows that M_s values are consistently lower in all magnetic hydrotalcite-type materials when compared to Fe_3O_4. Furthermore, it is worth noting that M_s values increase at lower temperatures across all cases.

At 300 K, the M_s values display minimal changes in the synthesized materials and do not exhibit significant differences concerning the Me^{2+}/Me^{3+} ratio. These findings agree with the results reported by Chen *et al.* [21] for the Fe_3O_4@CuNiAl-LDH composite. Conversely, M_s values obtained at 50 K show notable variations in materials containing double divalent cations, as well as in relation to the Me^{2+}/Me^{3+} ratio at this analysis temperature.

The alteration of Fe_3O_4 magnetic properties when combined with hydrotalcite-type materials can be attributed to the coating of LDH sheets on the Fe_3O_4 core. This phenomenon is a consequence of the decorated structure, where the sheets may adopt a vertical orientation. This orientation is predominantly associated with the synthesis method, particularly influenced by the choice of solvent used for dispersing the Fe_3O_4 nanoparticles in the water/

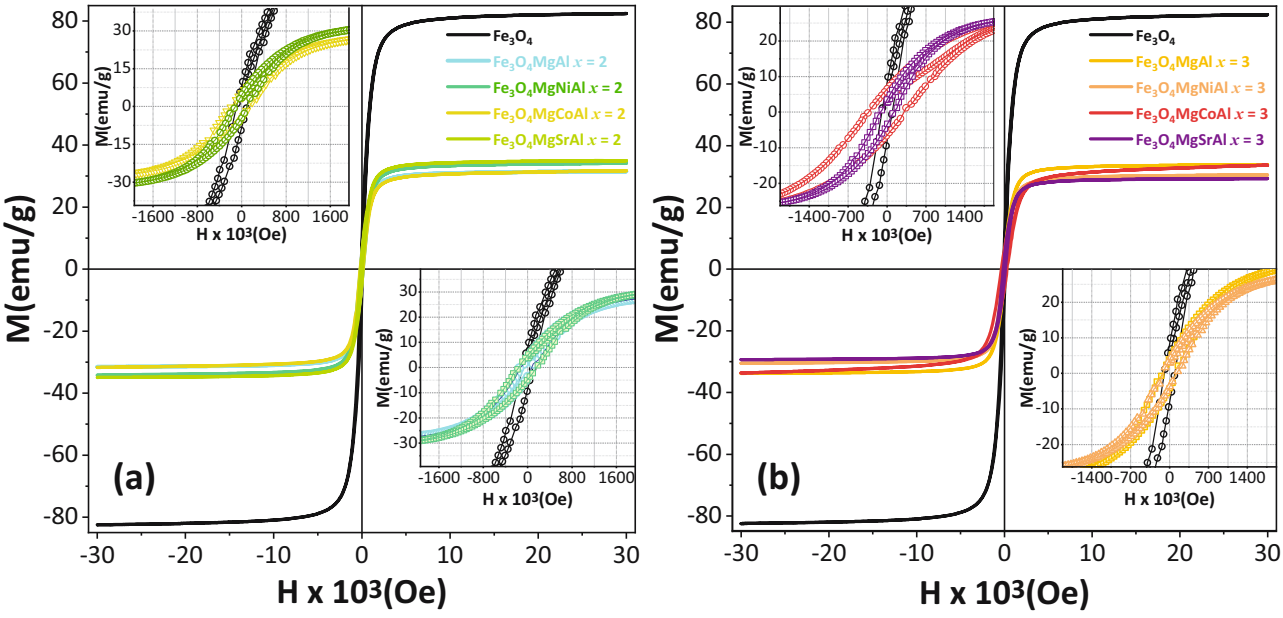

Figure 6: Temperature dependence of magnetization ZFC-FC measured at a 1 kOe applied field of the Fe_3O_4 magnetic hydrotalcite with molar ratios of (a) x = 2 and (b) x = 3 measured at room temperature (T = 300 K).

methanol solution (V water/V methanol = 1/1, v/v), which leads to this specific orientation [4]. The lower M_s values observed in magnetic hydrotalcites can be attributed to the high concentration of sheets covering the Fe_3O_4 nanoparticles. The M_r/M_s ratio, which indicates magnetic stability, is generally low (<0.2), suggesting superparamagnetic behavior in samples at 300 K. It was observed to decrease in the following order: Fe_3O_4–MgCoAl > Fe_3O_4-MgNiAl > Fe_3O_4–MgSrAl > Fe_3O_4–MgAl > Fe_3O_4 for Me^{2+}/Me^{3+} 2 and 3. This is related to the inter- and intragrain exchange interactions, sub-lattice magnetization, magnetic anisotropy, and morphology of the tested sample [60].

These results indicate that the magnetic, crystalline, and textural properties of the synthesized materials are strongly influenced by the ratio and nature of the divalent cations. In general, a smaller crystallite size with a larger surface area was observed in the materials, which indicates greater surface interactions, except for the Fe_3O_4MgSrAl system (Me^{2+}/M^{3+} = 3). This is because smaller particles have a higher surface/volume ratio, which increases the active area of the material. It was noted that the substitution of Mg^{2+} (0.72 Å), Co^{2+} (0.74 Å), and Ni^{2+} (0.69 Å) promotes the formation of layered structures due to their ionic radius similar to Fe^{3+} (0.78 Å). On the other hand, Sr^{2+} (1.18 Å) has a much larger ionic radius, which generates a structural disorder in the hydrotalcite. Thus, while Mg^{2+} stabilizes the structure and enhances the dispersion of Fe_3O_4, Co^{2+} and Ni^{2+} affect the magnetic properties by modifying anisotropy and coercivity. Sr^{2+}, due to its large size, tends to destabilize the network, decreasing the active surface and the magnetization, as seen in the small M_s values. The reduction in M_s in these samples may be due to surface effects, where the magnetic moments at the interface do not fully contribute to the magnetic order [61]. This structural modification improves the interaction with other molecules or reagents, which is particularly relevant for catalytic and adsorption applications [62].

These modifications directly influence the magnetic properties since the decrease in saturation magnetization (M_s) in the combined materials is associated with the presence of lamellar layers coating the magnetic nanoparticles. Furthermore, the remanence (M_r) and coercivity (H_c) show variations as a function of the type and proportion of the divalent cation, indicating that the structure affects the interaction between the magnetic domains. It is observed that samples with Ni^{2+} and Co^{2+} maintain relatively high M_s values compared to other substitutions, suggesting that these species favor the preservation of the magnetic ordering of Fe_3O_4. Nevertheless, the slight decrease in M_s with respect to the pure Fe_3O_4 sample could be related to the dilution of the Fe content in the crystal lattice and the possible formation of spinel phases with lower magnetic moment. Furthermore, the increase in the M_r/M_s ratio in samples with Co^{2+} indicates a higher magnetic anisotropy, suggesting a modification in the stability of the magnetic domains [63]. On the other hand, the introduction of Sr^{2+} generates a greater decrease in M_s, possibly due to its large ionic radius, which induces structural distortions and reduces the amount of effective ferromagnetic interactions [36]. Furthermore, the increase in H_c in some samples with Sr^{2+} indicates greater structural disorder, which affects the inversion dynamics of the magnetic domains and their stability. In this context, the adjustment in the molar composition of cations during the synthesis of hydrotalcites allows modulating the crystalline structure, as well as their textural and magnetic properties, offering precise control over the behavior of these materials in various applications.

Table 4: Magnetic parameters obtained from the hysteresis loops for the Fe_3O_4 magnetic hydrotalcite with molar ratios of x = 2 and x = 3 at 50 K and 300 K

Sample	Me^{2+}/Me^{3+}	M_s		M_r		M_r/M_s		H_c	
		50 K (emu/g)	300 K	50 K (emu/g)	300 K	50 K	300 K	50 K (Oe)	300 K
Fe_3O_4	—	89.47	82.23	13.014	7.91	0.15	0.10	0.089	0.008
Fe_3O_4MgAl	2	34.3	31.54	5.52	3.79	0.16	0.12	0.031	0.040
	3	34.24	32.43	5.81	3.19	0.17	0.10	0.060	0.080
Fe_3O_4MgCoAl	2	37.79	31.7	7.45	5.26	0.20	0.17	0.053	0.003
	3	33.67	31.6	6.42	4.13	0.19	0.13	0.053	0.090
Fe_3O_4MgNiAl	2	39.96	34.25	7.01	4.8	0.18	0.14	0.072	0.016
	3	48.25	30.54	8.07	3.66	0.17	0.12	0.064	0.017
Fe_3O_4MgSrAl	2	38.16	34.96	6.71	4.62	0.18	0.13	0.011	0.066
	3	32.13	29.34	5.43	3.31	0.17	0.11	0.023	0.017

4 Conclusions

Novel hydrotalcite-structured magnetic samples with 2 and 3 Me^{2+}/Me^{3+} molar ratios have been directly assembled by coprecipitation, with Co^{2+}, Ni^{2+}, and Sr^{2+} incorporation. The adjustment in the molar composition of metal cations during the synthesis of hydrotalcites allows the modulation of the crystalline structure, as well as their textural and magnetic properties. XRD analysis confirmed the formation of hydrotalcite and the integration of Fe_3O_4 particles in the synthesized samples, with structural parameters validated by Rietveld refinement. The variation in the molar ratio of metal cations influences the interlamellar distance and crystallite size of Fe_3O_4, with a secondary $SrCO_3$ phase observed in Sr^{2+} samples. The synthesis conditions affect the phase distribution, impacting the magnetic and catalytic properties of the composite material, and demonstrating an effective integration of Fe_3O_4 nanoparticles in the hydrotalcite matrix. The characteristic functional groups of magnetic hydrotalcites with 2 and 3 Me^{2+}/Me^{3+} molar ratios found were CO_3^{2-}/NO_3^-, OH, Al–O, Al–O–Al, Fe–O, Me–O–Me, and Sr–O, as identified by FTIR analysis. The SEM images show agglomerated particles of hexagonal platelets with nanometric spherical morphology in all samples. Increasing the Me^{2+}/Me^{3+} ratio tends to increase the particle size, especially when Ni^{2+} and Sr^{2+} are incorporated, whereas a lower Me^{2+}/Me^{3+} ratio is associated with smaller and better controlled particle sizes, particularly in the presence of Mg^{2+} and Al^{3+}. Large surface areas of 160 and 145 m^2/g were obtained for Fe_3O_4MgCoAl x = 3 and Fe_3O_4MgNiAl x = 3, respectively. The magnetization curves show no hysteresis, coercivity, and remanence in any sample, including Fe_3O_4, indicating good superparamagnetic behavior. The present high surface area magnetic samples and their facile synthesis approach can be utilized in a wide variety of hierarchical core–shell nanocomposites for potential utilization in the fields of catalysis, adsorption, and separation. The contribution of cations to the formation of the spine structure is closely related to their ionic size and charge. Divalent cations (such as Mg^{2+}, Ni^{2+}, Co^{2+}, and Sr^{2+}) can partially replace ferric cations in the structure, affecting both the crystallite size and the stability of the spinel phase.

Acknowledgments: E.N., G.S. and G.P.R. are grateful to CONICET (PIP 0111), UNLP (X941 - A 349), this work was also supported by MINCIENCIAS (Grant No 933-2023), and the Research Directorate of the Universidad Pedagógica y Tecnológica de Colombia for financial support.

Funding information: E.N., G.S., and G.P.R. are grateful to CONICET (PIP 0111), UNLP (X941 – A 349). This work was also supported by MINCIENCIAS (Grant No, 933-2023) and the Research Directorate of the Universidad Pedagógica y Tecnológica de Colombia for financial support.

Author contributions: Eliana Nope: formal analysis, investigation, methodology, supervision, visualization, writing – original draft, and review and editing. Gabriel Sathicq: writing – review and editing. José J. Martinez: methodology, writing – review and editing. Indry Milena Saavedra Gaona: formal analysis, visualization, and writing – original draft. Michael Castaneda Mendoza: formal analysis, visualization, and writing – original draft. Carlos Arturo Parra Vargas: resources, supervision, and writing – review and editing. Gustavo P. Romanelli: writing – review and editing. Rafael Luque: sources, visualization, and writing – review and editing. All authors have accepted responsibility for the entire content of this manuscript and approved its submission.

Conflict of interest: The authors state no conflict of interest.

Data availability statement: All data generated or analyzed during this study are included in this published article.

References

[1] Liu Z, Gao X, Liu B, Ma Q, Zhao T, Zhang J. Recent advances in thermal catalytic CO_2 methanation on hydrotalcite-derived catalysts. Fuel. 2022;321:124115.
[2] Gu Z, Atherton JJ, Xu ZP. Hierarchical layered double hydroxide nanocomposites: Structure, synthesis and applications. Chem Commun. 2015;51:3024–36.
[3] Bernard E, Zucha WJ, Lothenbach B, Mäder U. Stability of hydrotalcite (Mg-Al layered double hydroxide) in presence of different anions. Cem Concr Res. 2022;152:106674.
[4] Simeonidis K, Kaprara E, Rivera-Gil P, Xu R, Teran FJ, Kokkinos E, et al. Hydrotalcite-embedded magnetite nanoparticles for hyperthermia-triggered chemotherapy. Nanomaterials. 2021;11:1796.
[5] Zhu B, Chen L, Yan T, Xu J, Wang Y, Chen M, et al. Fabrication of Fe_3O_4/MgAl-layered double hydroxide magnetic composites for the effective removal of Orange II from wastewater. Water Sci Technol. 2018;78:1179–88.
[6] Shaw R, Kumar A. Hydrotalcite-based catalysts for 1,4-conjugate addition in organic synthesis. Catal Sci Technol. 2024;14:2090–104.
[7] Maggetti C, Pinelli D, Di Federico V, Sisti L, Tabanelli T, Cavani F, et al. Development and validation of an adsorption process for phosphate removal and recovery from municipal wastewater based on hydrotalcite-related materials. Sci Total Environ. 2024;951:175509.
[8] Ur Rehman M, Yin R, Yang Z-D, Zhang G, Liu Y, Zhang FM, et al. Fabrication and modification of hydrotalcite-based photocatalysts and their composites for CO_2 reduction: A critical review. ChemSusChem. 2025;18(10):e202402333.

[9] Jin W, Lee D, Jeon Y, Park DH. Biocompatible hydrotalcite nanohybrids for medical functions. Minerals. 2020;10:172.
[10] Burange AS, Gopinath CS. Catalytic applications of hydrotalcite and related materials in multi -component reactions: Concepts, challenges and future scope. Sustain Chem Pharm. 2021;22:100458.
[11] Bi X, Fan T, Zhang H. Novel morphology-controlled hierarchical core@shell structural organo-layered double hydroxides magnetic nanovehicles for drug release. ACS Appl Mater Interfaces. 2014;6:20498–509.
[12] Colombo M, Carregal-Romero S, Casula MF, Gutiérrez L, Morales MP, Böhm IB, et al. Biological applications of magnetic nanoparticles. Chem Soc Rev. 2012;41:4306–34.
[13] Qureshi AA, Javed S, Javed HMA, Akram A, Mustafa MS, Ali U, et al. Facile formation of SnO_2–TiO_2 based photoanode and Fe_3O_4@rGO based counter electrode for efficient dye-sensitized solar cells. Mater Sci Semicond Process. 2021;123:105545. doi: 10.1016/j.mssp.2020.105545.
[14] Albalawi AE, Khalaf AK, Alyousif MS, Alanazi AD, Baharvand P, Shakibaie M, et al. Fe_3O_4@piroctone olamine magnetic nanoparticles: Synthesize and therapeutic potential in cutaneous leishmaniasis. Biomed Pharmacother. 2021;139:111566.
[15] Anbarani MZ, Ramavandi B, Bonyadi Z. Modification of Chlorella vulgaris carbon with Fe_3O_4 nanoparticles for tetracycline elimination from aqueous media. Heliyon. 2023;9:e14356.
[16] Baladi M, Amiri M, Salavati-Niasari M. Green sol–gel auto-combustion synthesis, characterization and study of cytotoxicity and anticancer activity of $ErFeO_3$/Fe_3O_4/rGO nanocomposite. Arab J Chem. 2023;16:104575.
[17] Hasan G, Mohammed H, Althamthami M, et al. Synergistic effect of novel biosynthesis SnO_2@Fe_3O_4 nanocomposite: A comprehensive study of its photocatalytic of Dyes & antibiotics, antibacterial, and antimutagenic activities. J Photochem Photobiol A: Chem. 2023;443:114874. doi: 10.1016/j.jphotochem.2023.114874.
[18] Shao M, Ning F, Zhao J, Wei M, Evans DG, Duan X. Preparation of Fe_3O_4@SiO_2@layered double hydroxide core-shell microspheres for magnetic separation of proteins. J Am Chem Soc. 2012;134:1071–7.
[19] Huang Y, Mu G, Huan W, Yang Y, Yuan H, Batool I, et al. Degradation of TeCG catalyzed by graphene quantum Dot-reconstituted magnetic hydrotalcite composites. Chem Eng J. 2025;507:160749.
[20] Hu L, Li Z, Huang X, Zhu J, Hussaini I, He J, et al. Enhanced adsorption performance of modified hydrotalcite with CuO for nitrate in wastewater. J Electron Mater. 2025;54:2167–79.
[21] Chen X, Mi F, Zhang H, Zhang H. Facile synthesis of a novel magnetic core-shell hierarchical composite submicrospheres Fe_3O_4@CuNiAl-LDH under ambient conditions. Mater Lett. 2012;69:48–51.
[22] Zhang H, Zhang G, Bi X, Chen X. Facile assembly of a hierarchical core@shell Fe_3O_4@CuMgAl-LDH (layered double hydroxide) magnetic nanocatalyst for the hydroxylation of phenol. J Mater Chem A. 2013;1:5934–42.
[23] Nope E, Sathicq ÁG, Martínez JJ, Rojas HA, Luque R, Romanelli GP. Ternary hydrotalcites in the multicomponent synthesis of 4H-Pyrans. Catalysts. 2020;10:70.
[24] Kang YS, Risbud S, Rabolt JF, Stroeve P. Synthesis and characterization of nanometer-size Fe_3O_4 and γ-Fe_2O_3 particles. Chem Mater. 1996;8:2209–11.
[25] Niculescu A-G, Chircov C, Grumezescu AM. Magnetite nanoparticles: Synthesis methods – A comparative review. Methods. 2022;199:16–27.
[26] Dudchenko N, Pawar S, Perelshtein I, Fixler D. Magnetite nanoparticles: Synthesis and applications in optics and nanophotonics. Materials. 2022;15:2601.
[27] Nope E, Sathicq ÁG, Martínez JJ, ALOthman ZA, Romanelli GP, Nares EM, et al. Revisiting hydrotalcite synthesis: Efficient combined mechanochemical/coprecipitation synthesis to design advanced tunable basic catalysts. Nanotechnol Rev. 2024;13(1):20240042. doi: 10.1515/ntrev-2024-0042.
[28] Jurišová J, Danielik V, Malečková S, Guzikiewiczová E, Králik M, Vizárová K, et al. Preparation and characterisation of hydrotalcites colloid dispersions suitable for deacidification of paper information carriers. Chem Pap. 2024;78:1719–30.
[29] Nagarjuna R, Challagulla S, Sahu P, Roy S, Ganesan R. Polymerizable sol–gel synthesis of nano-crystalline WO_3 and its photocatalytic Cr(VI) reduction under visible light. Adv Powder Technol. 2017;28(12):3265–73. doi: 10.1016/j.apt.2017.09.030.
[30] Elías VR, Sabre EV, Winkler EL, Casuscelli SG, Eimer GA. On the nature of Cr species on MCM-41 obtained by a one step method and their enhanced photocatalytic performance under visible radiation: New insights by a combined techniques approach. Appl Catal A: Gen. 2013;467:363–70.
[31] Salimi M, Zamanpour A. Ag nanoparticle immobilized on functionalized magnetic hydrotalcite (Fe_3O_4/HT-SH-Ag) for clean oxidation of alcohols with TBHP. Inorg Chem Commun. 2020;119:108081.
[32] Salimi M, Esmaeli-nasrabadi F, Sandaroos R. Fe_3O_4@Hydrotalcite-NH_2-CoII NPs: A novel and extremely effective heterogeneous magnetic nanocatalyst for synthesis of the 1-substituted 1H-1, 2, 3, 4-tetrazoles. Inorg Chem Commun. 2020;122:108287.
[33] Monshi A, Foroughi MR, Monshi MR. Modified Scherrer equation to estimate more accurately nano-crystallite size using XRD. World J Nano Sci Eng. 2012;2:154–60.
[34] Mustapha S, Ndamitso MM, Abdulkareem AS, Tijani JO, Shuaib DT, Mohammed AK, et al. Comparative study of crystallite size using Williamson-Hall and Debye-Scherrer plots for ZnO nanoparticles. Adv Nat Sci: Nanosci Nanotechnol. 2019;10:045013.
[35] Saavedra Gaona IM, Mendoza MC, Vargas CAP. Structural and magnetic properties of $Nd_3Ba_5Cu_8O_{18+\delta}$ superconductor. J Low Temp Phys. 2023;211:156–65.
[36] Saavedra Gaona IM, Supelano GI, Suarez Vera SG, Fonseca LCI, Castaneda Mendoza M, Sánchez Saenz CL, et al. Magnetic and electrical behaviour of Yb substitution on $Bi_{1-x}Yb_xFeO_3$ ($0.00 < x < 0.06$) ceramic system. J Magn Magn Mater. 2024;593:171827.
[37] Ros FC. Rietveld refinement strategy of $CaTa_{4-x}Nb_xO_{11}$ solid solutions using GSAS-EXPGUI software package. Mater Sci Forum. 2017;888:167–71.
[38] Murugesan S, Thirumurugesan R, Mohandas E, Parameswaran P. X-ray diffraction Rietveld analysis and Bond Valence analysis of nano titania containing oxygen vacancies synthesized *via* sol-gel route. Mater Chem Phys. 2019;225:320–30.
[39] Cuervo Farfán JA. Producción y propiedades físicas de nuevas perovskitas complejas del tipo RAMOX (R = La, Nd, Sm, Eu; A = Sr, Bi; M = Ti, Mn, Fe). PhD thesis. Universidad Nacional de Colombia. https://repositorio.unal.edu.co/handle/unal/79915. (2021, accessed 15 August 2024).
[40] Naranjo CEE, Hernandez JST, Salgado MJR, Tabares JA, Maccari F, Cortes A, et al. Processing and characterization of $Nd_2Fe_{14}B$

microparticles prepared by surfactant-assisted ball milling. Appl Phys A. 2018;124:564.
[41] Abd-Elnaiem AM, Hakamy A, Afify N, Omer M, Abdelbaki RF. Nanoarchitectonics of zinc nickel ferrites by the hydrothermal method for improved structural and magnetic properties. J Alloy Compd. 2024;984:173941.
[42] Sharma SK, Kushwaha PK, Srivastava VK, Bhatt SD, Jasra RV. Effect of hydrothermal conditions on structural and textural properties of synthetic hydrotalcites of varying Mg/Al ratio. Ind Eng Chem Res. 2007;46:4856–65.
[43] Kloprogge JT, Frost RL. Fourier transform infrared and Raman spectroscopic study of the local structure of Mg-, Ni-, and Co-hydrotalcites. J Solid State Chem Fr. 1999;146:506–15.
[44] Julianti NK, Wardani TK, Gunardi I. Effect of calcination at synthesis of Mg-Al hydrotalcite using co-precipitation method. J Pure Appl Chem Res. 2017;6:7–13.
[45] Mehta K, Jha MK, Divya N. Statistical optimization of biodiesel production from Prunus armeniaca oil over strontium functionalized calcium oxide. Res Chem Intermed. 2018;44:7691–709.
[46] Yan Q, Zhang Z, Zhang Y, Umar A, Guo Z, O'Hare D, et al. Hierarchical Fe_3O_4 core–shell layered double hydroxide composites as magnetic adsorbents for anionic dye removal from wastewater. Eur J Inorg Chem. 2015;2015:4182–91.
[47] Zhang Y, Niu S, Han K, Li Y, Lu C. Synthesis of the SrO–CaO–Al_2O_3 trimetallic oxide catalyst for transesterification to produce biodiesel. Renew Energy. 2021;168:981–90.
[48] Ikram M, Haider A, Imran M, Haider J, Naz S, Ul-Hamid A, et al. Facile synthesis of starch and tellurium doped SrO nanocomposite for catalytic and antibacterial potential: In silico molecular docking studies. Int J Biol Macromol. 2022;221:496–507.
[49] Wu Q, Olafsen A, Vistad ØB, Roots J, Norby P. Delamination and restacking of a layered double hydroxide with nitrate as counter anion. J Mater Chem. 2005;15:4695–700.
[50] Yan LG, Yang K, Shan RR, Yan T, Wei J, Yu SJ, et al. Kinetic, isotherm and thermodynamic investigations of phosphate adsorption onto core-shell Fe_3O_4@LDHs composites with easy magnetic separation assistance. J Colloid Interface Sci. 2015;448:508–16.
[51] Thongtem T, Tipcompor N, Phuruangrat A, Thongtem S. Characterization of $SrCO_3$ and $BaCO_3$ nanoparticles synthesized by sonochemical method. Mater Lett. 2010;64:510–2.
[52] Aisawa S, Hirahara H, Uchiyama H, Takahashi S, Narita E. Synthesis and thermal decomposition of Mn–Al layered double hydroxides. J Solid State Chem. 2002;167:152–9.
[53] Wiyantoko B, Kurniawati P, Purbaningtias TE, Fatimah I. Synthesis and characterization of hydrotalcite at different Mg/Al molar ratios. Procedia Chem. 2015;17:21–6.
[54] Shekoohi K, Hosseini FS, Haghighi AH, Sahrayian A. Synthesis of some Mg/Co-Al type nano hydrotalcites and characterization. Methods X. 2017;4:86–94.
[55] Durgalakshmi D, Ajay Rakkesh R, Kamil S, Karthikeyan S, Balakumar S. Rapid dilapidation of alcohol using magnesium oxide and magnesium aspartate based nanostructures: A Raman spectroscopic and molecular simulation approach. J Inorg Organomet Polym. 2019;29:1390–9.
[56] Gao G, Zhu Z, Zheng J, Liu Z, Wang Q, Yan Y. Ultrathin magnetic Mg-Al LDH photocatalyst for enhanced CO_2 reduction: Fabrication and mechanism. J Colloid Interface Sci. 2019;555:1–10.
[57] Karthikeyan C, Karuppuchamy S. Transesterification of Madhuca longifolia derived oil to biodiesel using Mg–Al hydrotalcite as heterogeneous solid base catalyst. Mater Focus. 2017;6:101–6.
[58] Szymaszek-Wawryca A, Summa P, Duraczyńska D, Díaz U, Motak M. Hydrotalcite-modified clinoptilolite as the catalyst for selective catalytic reduction of NO with ammonia (NH_3-SCR). Materials. 2022;15:7884.
[59] Galindo R, López-Delgado A, Padilla I, Yates M. Synthesis and characterisation of hydrotalcites produced by an aluminium hazardous waste: A comparison between the use of ammonia and the use of triethanolamine. Appl Clay Sci. 2015;115:115–23.
[60] Shafi KVPM, Gedanken A, Prozorov R, Balogh J. Sonochemical preparation and size-dependent properties of nanostructured $CoFe_2O_4$ particles. Chem Mater. 1998;10:3445–50.
[61] Stamate A-E. Layered double hydroxide-based catalysts for fine organic synthesis. Phd thesis. University of Bucharest; Doctoral School in Chemistry. https://theses.hal.science/tel-03906532. (2022, accessed 11 February 2025).
[62] Baños JGC, Lara VEN, Puentes CO. Magnetita (Fe_3O_4): Una estructura inorgánica con múltiples aplicaciones en catálisis heterogénea. Rev Colomb Quím. 2017;46:42–59.
[63] Yang Sun(孙洋) RL. Impact of Co^{2+} substitution on structure and magnetic properties of M-type strontium ferrite with different Fe/Sr ratios. Chin Phys B. 2024;33:107506.